

Linear Analysis of the Evolution of Nearly Polar Low Mass Circumbinary Discs

Stephen H. Lubow¹  and Rebecca G. Martin² 

¹*Space Telescope Science Institute, 3700 San Martin Drive, Baltimore, MD 21218, USA*

²*Department of Physics and Astronomy, University of Nevada, Las Vegas, 4505 South Maryland Parkway, Las Vegas, NV 89154, USA*

Accepted XXX. Received YYY; in original form ZZZ

ABSTRACT

[Martin & Lubow \(2017\)](#) showed through simulations that an initially tilted disc around an eccentric binary can evolve to polar alignment in which the disc lies perpendicular to the binary orbital plane. We apply linear theory to show both analytically and numerically that a nearly polar aligned low mass circumbinary disc evolves to polar alignment and determine the alignment timescale. Significant disc evolution towards the polar state around moderately eccentric binaries can occur for typical protostellar disc parameters in less than a typical disc lifetime for binaries with orbital periods of order 100 years or less. Resonant torques are much less effective at truncating the inner parts of circumbinary polar discs than the inner parts of coplanar discs. For polar discs, they vanish for a binary eccentricity of unity. The results agree with the simulations in showing that discs can evolve to a polar state. Circumbinary planets may then form in such discs and reside on polar orbits.

Key words: accretion, accretion discs – binaries: general – hydrodynamics – planets and satellites: formation

1 INTRODUCTION

Observations of protostellar circumbinary discs have revealed misalignments between the orbital planes of the binaries and their discs in some cases. For example, the peculiar light

* E-mail: lubow@stsci.edu

† E-mail: rebecca.martin@unlv.edu

curve of KH 15D can be explained by a misaligned precessing disc (e.g. [Winn et al. 2004](#); [Chiang & Murray-Clay 2004](#); [Capelo et al. 2012](#)). The binary protostar IRS 43 has a misalignment greater than 60° between the binary and the disc ([Brinch et al. 2016](#)). Binary GG Tau may be misaligned by $25^\circ - 30^\circ$ from its circumbinary disc ([Cazzoletti et al. 2017](#)). The debris disc around 99 Herculis is most likely perpendicular to the binary orbital plane ([Kennedy et al. 2012](#)).

There are some mechanisms that could explain how misalignments could arise between circumbinary discs and their central binary orbital planes. Turbulence in a star-forming gas cloud could result in disc misalignments with the central binary ([Offner et al. 2010](#); [Tokuda et al. 2014](#); [Bate 2012](#)). If a young binary star system accretes material after its formation process, the material is likely to be misaligned with the binary orbit and so misaligned discs may form around young binary stars ([Bate et al. 2010](#)). In addition, misalignment can be the result of binary star formation from an elongated cloud whose axes are misaligned with respect to the cloud rotation axis (e.g. [Bonnell & Bastien 1992](#)). Such misalignment mechanisms likely apply to both circumstellar and circumbinary discs.

The Kepler telescope has detected about a dozen extra-solar circumbinary planets (e.g., [Doyle et al. 2011](#); [Welsh et al. 2015](#); [Kostov et al. 2016](#)). Such planets likely formed in a circumbinary disc. The planets found to date are nearly coplanar with the binary orbit. It would be useful to know if there are possible long lived misaligned circumbinary discs that could result in the formation of noncoplanar circumbinary planets.

Previous analytic and numerical studies of the tilt evolution of circumstellar and circumbinary discs have largely focused on the alignment process towards the binary orbital plane (e.g., [Papaloizou & Terquem 1995](#); [Larwood & Papaloizou 1997](#); [Lubow & Ogilvie 2000](#); [Nixon et al. 2011](#); [Facchini et al. 2013](#); [Lodato & Facchini 2013](#); [Foucart & Lai 2013, 2014](#)). It is natural to expect that tilted discs will evolve towards alignment with the binary since such a configuration would have minimum energy for a fixed density distribution. In presence of dissipation, one would expect evolution to coplanar alignment with the binary orbit. A notable exception is the study by [Aly et al. \(2015\)](#) who found that disc alignment can occur perpendicular to the binary orbital plane in the context of a cool disc that undergoes tearing around a supermassive black hole binary. We are interested in warmer discs that are found in the protostellar/protoplanetary context.

Binary-disc resonances can play a role in causing a circumstellar disc to not achieve a

coplanar configuration (Lubow 1992; Papaloizou & Terquem 1995; Lubow & Ogilvie 2000). However, these effects are either weak or are restricted to certain disc parameters.

Recently, we showed through smoothed particle hydrodynamic (SPH) simulations that a somewhat misaligned low mass protostellar circumbinary disc can evolve to an apparently stable polar state in which the disc plane is perpendicular to the orbital plane of the binary (Martin & Lubow 2017). A key ingredient is that the binary be on an eccentric orbit. In this polar orientation, the rotation axis of the disc is parallel to the eccentricity vector of the binary.

A misaligned test (massless) particle orbit around a circular orbit binary undergoes nodal precession. The angular momentum vector of the test particle precesses about the binary angular momentum vector. Similarly, a misaligned protostellar disc around a circular orbit binary can undergo the same form of precession. A protostellar disc is often able to hold itself together and precess as a solid body (e.g., Papaloizou & Terquem 1995; Larwood & Papaloizou 1997; Lubow & Ogilvie 2000; Foucart & Lai 2014). Differential precession across a disc can cause it to become highly warped. But protostellar discs are often warm enough for global radial communication to occur through pressure induced bending waves that permit the disc to resist warping. Dissipation within the disc leads to alignment with the binary orbital plane.

For eccentric orbit binaries, test particle orbits behave somewhat differently. Instead of precessing about the orbital axis of the binary, they can instead precess about the eccentricity vector of the binary that lies perpendicular to the binary angular momentum axis (Farago & Laskar 2010; Doolin & Blundell 2011; Li et al. 2014). There is a critical initial inclination above which the transition occurs from precessing about the orbital axis of the binary to precessing about the eccentricity vector of the binary. The critical misalignment angle depends upon the eccentricity of the binary and the longitude of the ascending node of the particle's orbit. Polar alignment of a moderately misaligned low mass disc can be understood in terms of transitions between these precessing orbits to a nonprecessing polar state as the disc undergoes tidal dissipation (Martin & Lubow 2017).

The stability of nearly polar discs or rings has been explored in the context of galaxies and planets. Polar rings are observed around galaxies (Schweizer et al. 1983; Combes 2014; Iodice et al. 2015). Their frequency around galaxies is estimated to be $\sim 5\%$, after various selection effects are taken into account (Whitmore et al. 1990). There are several models for the origin of polar rings in galaxies that generally involve the gravitational effects of

dark matter halos acting on infalling material (gas or galaxies). In one early model, the ring attains a polar configuration through the effects of a spheroidal or triaxial potential acting on a dissipative gaseous ring (Durisen et al. 1983; Steiman-Cameron & Durisen 1990). Such a configuration is similar to the eccentric binary case, in which the time-averaged potential has a triaxial form (Farago & Laskar 2010). In a completely different context, Dobrovolskis et al. (1989) showed that a possible polar ring around Neptune would be stable through similar arguments.

In this paper, we analyze the dynamics of a nearly polar circumbinary disc about an eccentric binary. A tilted protostellar disc is subject to the development of bending waves that are communicated by pressure which has not been previously considered in models of polar discs. In addition, Keplerian discs experience a near resonance of horizontal epicyclic motions driven by horizontal pressure gradients in a warped disc (Papaloizou & Pringle 1983).

As we were completing the work on this paper, a preprint by Zanazzi & Lai (2017) appeared on this topic. Our paper has a somewhat different emphasis. Both papers agree that the polar state is stable and obtain similar tilt evolution timescales.

The outline of the paper is as follows. Section 1 contains the introduction. Section 2 describes the linear equations used to model the evolution of a nearly polar disc. Section 3 describes solutions to those equations based on an expansion in which the tidal potential is weak. Section 4 discusses numerically determined modes for nearly polar discs. Section 5 analyzes the tidal truncation of the inner parts of a polar circumbinary disc. Section 6 briefly discusses the stability of a disc that is perpendicular to the binary orbital plane and the polar disc plane. Section 7 discusses some energetics issues related to polar discs. Section 8 contains a summary.

2 NEARLY POLAR DISC MODEL

We consider an eccentric binary with component stars that have masses M_1 and M_2 and total mass $M = M_1 + M_2$ in an orbit with semi-major axis a_b and eccentricity e_b . We are interested in nearly polar, low mass circumbinary discs. Such discs have their angular momentum vectors nearly parallel (or antiparallel) to their binary eccentricity vectors that point from the binary centers of mass towards their binary pericenters. In this configuration, the disc is nearly perpendicular the binary orbital plane. To describe this configuration, we

define a Cartesian coordinate system (x, y, z) whose origin is at the binary center of mass and with the y -axis parallel to the binary angular momentum \mathbf{J}_b and the z -axis parallel to the binary eccentricity vector \mathbf{e}_b . We consider the disc to be composed of circular rings with surface density $\Sigma(r)$ whose orientations vary with radius r and orbit with Keplerian angular speed $\Omega(r)$. We denote the unit vector parallel to the ring angular momentum at each radius by (ℓ_x, ℓ_y, ℓ_z) . We consider small departures of the disc from the $x - y$ plane, so that $|\ell_x| \ll 1$, $|\ell_y| \ll 1$, and $\ell_z \approx 1$.

We apply equations (12) and (13) in Lubow & Ogilvie (2000) for the evolution of the disc 2D tilt vector $\boldsymbol{\ell}(r, t) = (\ell_x, \ell_y)$ and 2D internal torque $\mathbf{G}(r, t) = (G_x, G_y)$. The tilt evolution equation is given by

$$\Sigma r^2 \Omega \frac{\partial \boldsymbol{\ell}}{\partial t} = \frac{1}{r} \frac{\partial \mathbf{G}}{\partial r} + \mathbf{T}, \quad (1)$$

where \mathbf{T} is the tidal torque per unit area due to the eccentric binary whose orbit lies in the $x - z$ plane. Equation (13) in Lubow & Ogilvie (2000) provides the internal torque evolution equation

$$\frac{\partial \mathbf{G}}{\partial t} - \omega_a \mathbf{e}_z \times \mathbf{G} + \alpha \Omega \mathbf{G} = \frac{\mathcal{I} r^3 \Omega^3}{4} \frac{\partial \boldsymbol{\ell}}{\partial r}, \quad (2)$$

where α is the usual turbulent viscosity parameter, $\omega_a(r)$ is the apsidal precession rate for a disc that is polar that is given in Equation (A16) of Appendix A, and

$$\mathcal{I} = \int \rho z^2 dz, \quad (3)$$

for disc density $\rho(r)$. We apply boundary conditions that the internal torque vanishes at the inner and outer disc edges r_{in} and r_{out} , respectively. That is,

$$\mathbf{G}(r_{\text{in}}, t) = \mathbf{G}(r_{\text{out}}, t) = 0. \quad (4)$$

This is a natural boundary condition because the internal torque vanishes just outside the disc boundaries. Thus, any smoothly varying internal torque would need to satisfy this condition.

The torque term due to the eccentric binary follows from an application of equations (2.17) and (2.18) in Farago & Laskar (2010). Note that we apply a different coordinate system in which our (x, y, z) coordinates corresponds to their (y, z, x) coordinates. The torque term is expressed as

$$\mathbf{T} = \Sigma r^2 \Omega \boldsymbol{\tau} \quad (5)$$

with

$$\boldsymbol{\tau} = (a(r)\ell_y, b(r)\ell_x) \quad (6)$$

and

$$a(r) = -(1 + 4e_b^2) \omega_p(r), \quad (7)$$

and

$$b(r) = 5e_b^2 \omega_p(r), \quad (8)$$

where frequency ω_p is given by

$$\omega_p(r) = \frac{3}{4} \frac{\beta}{M} \left(\frac{a_b}{r} \right)^{7/2} \Omega_b, \quad (9)$$

and β is the reduced mass

$$\beta = \frac{M_1 M_2}{M_1 + M_2}. \quad (10)$$

We seek solutions of the form $\boldsymbol{\ell} \propto e^{i\omega t}$ and $\mathbf{G} \propto e^{i\omega t}$ and Equations (1) and (2) become

$$i\omega \Sigma r^2 \Omega \boldsymbol{\ell} = \frac{1}{r} \frac{d\mathbf{G}}{dr} + \Sigma r^2 \Omega \boldsymbol{\tau} \quad (11)$$

and

$$i\omega \mathbf{G} - \omega_a \mathbf{e}_z \times \mathbf{G} + \alpha \Omega \mathbf{G} = \frac{\mathcal{I} r^3 \Omega^3}{4} \frac{d\boldsymbol{\ell}}{dr}, \quad (12)$$

respectively.

3 NEARLY RIGID DISC EXPANSION

3.1 Lowest order

We apply the nearly rigid tilted disc expansion procedure in [Lubow & Ogilvie \(2000\)](#). We expand variables in the tidal potential that is considered to be weak as follows:

$$\begin{aligned} a &= A^{(1)}, \\ b &= B^{(1)}, \\ \boldsymbol{\ell} &= \boldsymbol{\ell}^{(0)} + \boldsymbol{\ell}^{(1)} + \dots, \\ \omega &= \omega^{(1)} + \omega^{(2)} + \dots, \\ \mathbf{G} &= \mathbf{G}^{(1)} + \mathbf{G}^{(2)} + \dots, \\ \boldsymbol{\tau} &= \boldsymbol{\tau}^{(1)} + \boldsymbol{\tau}^{(2)} + \dots, \end{aligned} \quad (13)$$

where a and b are given by Equations (7) and (8), respectively. a and b depend on the tidal potential and are regarded as first order quantities.

To lowest order, the disc is rigid and the tilt vector $\boldsymbol{\ell}^{(0)} = (\ell_x^{(0)}, \ell_y^{(0)})$ is constant in radius. We integrate r times Equation (11) over the entire disc and apply the boundary conditions

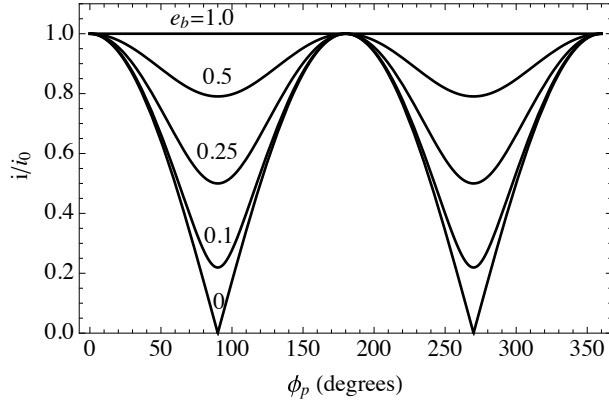


Figure 1. Normalized disc tilt angle relative to the polar orientation (Equation (19)) as a function of precession angle $\phi_p = \omega^{(1)}t$ for various values of binary eccentricity.

given by Equation (4) to obtain

$$\int_{r_{\text{in}}}^{r_{\text{out}}} \Sigma r^3 \Omega (i \omega^{(1)} \ell^{(0)} - \tau^{(1)}) dr = 0, \quad (14)$$

where

$$\tau^{(1)}(r) = (A^{(1)}(r) \ell_y^{(0)}, B^{(1)}(r) \ell_x^{(0)}). \quad (15)$$

We then obtain for the disc frequency in lowest order

$$\omega^{(1)} = \frac{3\sqrt{5}}{4} e_b \sqrt{1 + 4e_b^2} \frac{M_1 M_2}{M^2} \left\langle \left(\frac{a_b}{r} \right)^{7/2} \right\rangle \Omega_b, \quad (16)$$

where the bracketed term involves the angular momentum weighted average

$$\left\langle \left(\frac{a_b}{r} \right)^{7/2} \right\rangle = \frac{\int_{r_{\text{in}}}^{r_{\text{out}}} \Sigma r^3 \Omega (a_b/r)^{7/2} dr}{\int_{r_{\text{in}}}^{r_{\text{out}}} \Sigma r^3 \Omega dr}. \quad (17)$$

The tilt components are related by

$$\ell_y^{(0)} = -\frac{\sqrt{5} i e_b}{\sqrt{1 + 4e_b^2}} \ell_x^{(0)}. \quad (18)$$

Because $|\ell_x^{(0)}|$ and $|\ell_y^{(0)}|$ differ, the disc undergoes secular tilt oscillations with tilt variations $i(t)$ with respect to the $x - y$ plane. If we assume the disc is initially tilted along the x -axis (i.e., $\ell_x^{(0)}$ is real), then

$$i(t) = i(0) \sqrt{\frac{1 + 9e_b^2 + (1 - e_b^2) \cos(2\omega^{(1)}t)}{2(1 + 4e_b^2)}}. \quad (19)$$

Figure 1 plots the tilt as a function of precession angle $\phi_p = \omega^{(1)}t$ for various values of binary eccentricity. Tilt oscillations occur because the binary potential is nonaxisymmetric around the direction of the binary eccentricity vector (the z -axis). For $e_b = 1$, the oscillations are suppressed because the binary orbit is along a line and the potential is then axisymmetric about the line.

We integrate r times Equation (11) and apply boundary condition (4) to find the internal torque to lowest order

$$\mathbf{G}^{(1)}(r) = \int_{r_{\text{in}}}^r \Sigma r^3 \Omega (i\omega^{(1)} \boldsymbol{\ell}^{(0)} - \boldsymbol{\tau}^{(1)}) dr'. \quad (20)$$

Equation (12) in lowest order is given by

$$\alpha \Omega \mathbf{G}^{(1)} = \frac{1}{4} \mathcal{I} r^3 \Omega^3 \frac{d\boldsymbol{\ell}^{(1)}}{dr}. \quad (21)$$

This is used to determine $\boldsymbol{\ell}^{(1)}$.

3.2 Higher order

To next order in the nearly rigid tilt approximation, we determine the tilt oscillation amplitude decay rate $\text{Im}(\omega^{(2)})$. We show here analytically that the decay rate is positive, implying that the disc evolves to a polar state where $\boldsymbol{\ell} = 0$. Circumbinary disc dynamics involving an eccentric orbit binary is different from the case involving a circular orbit binary analyzed previously (e.g. [Facchini et al. 2013](#); [Foucart & Lai 2014](#)) because of the presence of secular tilt oscillations described by Equation (19).

We determine the deviations from the rigid tilt, i.e., the warp $\boldsymbol{\ell}^{(1)} = (\ell_x^{(1)}, \ell_y^{(1)})$, by integrating Equation (21) to obtain

$$\boldsymbol{\ell}^{(1)}(r) = \boldsymbol{\ell}^{(1)}(r_{\text{in}}) + \int_{r_{\text{in}}}^r \frac{4\alpha \mathbf{G}^{(1)}}{\mathcal{I} r'^3 \Omega^2} dr'. \quad (22)$$

In this linear analysis we are free to specify the value of one component of $\boldsymbol{\ell}(r_{\text{in}})$. We specify the value of $\ell_x(r_{\text{in}}) = \ell_x^{(0)}(r_{\text{in}})$ that is taken to be real quantity and consequently

$$\ell_x^{(1)}(r_{\text{in}}) = 0. \quad (23)$$

We take the dot product of Equation (11) with $r\boldsymbol{\ell}^*$ and integrate in radius over the disc to obtain

$$\begin{aligned} \text{Im}(\omega) \int_{r_{\text{in}}}^{r_{\text{out}}} \Sigma r^3 \Omega |\boldsymbol{\ell}|^2 dr &= - \int_{r_{\text{in}}}^{r_{\text{out}}} \Sigma r^3 \Omega \text{Re}(\boldsymbol{\tau} \cdot \boldsymbol{\ell}^*) dr \\ &+ \int_{r_{\text{in}}}^{r_{\text{out}}} \text{Re} \left(\mathbf{G} \cdot \frac{d\boldsymbol{\ell}^*}{dr} \right) dr, \end{aligned} \quad (24)$$

where the second term on the RHS is obtained by an integration by parts and the application of boundary conditions (4).

The first term on the RHS involves the dot product of the tidal torque with the disc tilt. The integrand involves term $\text{Re}(\boldsymbol{\tau} \cdot \boldsymbol{\ell}^*) = (a + b)\text{Re}(\ell_x \ell_y^*)$. For a purely precessional torque that involves no secular tilt oscillations, as occurs for a slightly tilted circumbinary disc that lies near the orbital plane of a circular orbit binary, we have that $a(r) = -b(r)$ in Equation

(6). It then immediately follows that the tidal torque term involving $Re(\boldsymbol{\tau} \cdot \boldsymbol{\ell}^*)$ vanishes in that case.

The contributions of the tidal torque term in Equation (24) are less clear in the case of a disc undergoing secular tilt oscillations, as occurs in the nearly polar case, where a and $-b$ differ. In fact, the contribution of this term does not vanish to all orders, as we show in Section 4.6 for numerically computed modes. It is easy to see that in zeroth order $Re(\ell_x^{(0)} \ell_y^{(0)*})$ vanishes using Equation (18) which implies that the tidal torque term vanishes in first order.

The internal torque term that appears as the second term on the RHS of Equation (24) is nonzero in second order, since to lowest order it involves the product $\mathbf{G}^{(1)} \cdot d\boldsymbol{\ell}^{(1)*}/dr$. To properly compare the tidal torque term with the internal torque term on the RHS of Equation (24), we must analyze the tidal torque term in second order.

We evaluate Equation (24) to second order as

$$\begin{aligned} Im(\omega^{(2)}) J_d |\boldsymbol{\ell}^{(0)}|^2 &= -2\pi \int_{r_{in}}^{r_{out}} \Sigma r^3 \Omega Re\left((\boldsymbol{\tau} \cdot \boldsymbol{\ell}^*)^{(2)}\right) dr \\ &+ 2\pi \int_{r_{in}}^{r_{out}} Re\left(\mathbf{G}^{(1)} \cdot \frac{d\boldsymbol{\ell}^{(1)*}}{dr}\right) dr, \end{aligned} \quad (25)$$

where J_d is the angular momentum of the disc

$$J_d = 2\pi \int_{r_{in}}^{r_{out}} \Sigma r^3 \Omega dr \quad (26)$$

and

$$Re\left((\boldsymbol{\tau} \cdot \boldsymbol{\ell}^*)^{(2)}\right) = (A^{(1)} + B^{(1)}) Re\left(\ell_x^{(1)} \ell_y^{(0)*} + \ell_x^{(0)} \ell_y^{(1)*}\right). \quad (27)$$

In Appendix B1 we show that in first order $Re(\ell_x \ell_y^*)$ is constant in radius. We then evaluate this constant at the disc inner edge and show that it is zero in Appendix B2. Finally, in Appendix B3 we show that the RHS of Equation (27) is zero at all radii in the disc. This occurs because $a(r)/b(r)$ is independent of radius. We then have that the LHS of Equation (25) balances the second term on the RHS. Applying Equation (21) we obtain

$$Im(\omega^{(2)}) = \frac{2\pi}{J_d |\boldsymbol{\ell}_0|^2} \int_{r_{in}}^{r_{out}} \frac{4\alpha |\mathbf{G}^{(1)}|^2}{I r^3 \Omega^2} dr. \quad (28)$$

This relation agrees with Equation (47) of Lubow & Ogilvie (2001) that was derived for a nearly coplanar disc that does not undergo secular tilt oscillations. The tilt amplitude evolution rate $Im(\omega^{(2)})$ then is positive definite which implies that a disc whose orientation is slightly different from polar will evolve towards the polar state. *Consequently, we find analytically that low mass polar discs are secularly linearly stable.*

Consider a set of discs of a fixed structure. That is, the temperature and density variations are fixed in radius with fixed inner and outer radii, but the temperature and density

normalization can vary. For example, if the temperature is a power law in radius, then the exponent in the power law is taken to be fixed, but the temperature at some reference radius, such as the disc inner edge, can change across discs. Equation (28) implies that for fixed disc structure, small departures of tilt from the polar state decay towards this state on a timescale

$$t_{\text{evol}} \propto \frac{(H/r)^2 \Omega_b}{\alpha(\omega^{(1)})^2} \quad (29)$$

$$\propto \frac{(H/r)^2 M^2}{\alpha e_b^2 (1 + 4e_b^2) M_1^2 M_2^2 \Omega_b}, \quad (30)$$

where H/r is the disc aspect ratio at some reference radius that we can take to be the disc inner radius. The full dependence (not assuming a fixed disc structure) is more complicated because the decay rate is sensitive to the disc inner radius that depends in turn on the binary mass ratio, H/r , α , and e_b , as is discussed later in Section 5.

4 NUMERICAL DETERMINATION OF MODES

4.1 Method

In this section, we present results of solving the linearized tilt Equations (11) and (12) numerically. We are again interested in the longest lived mode that is nearly a rigid tilt mode. We compare the numerical results with those of the expansion method in Section 3.

We numerically determine complex eigenfunctions $\ell(r)$ and G and eigenvalue ω in Equations (11) and (12) by a shooting method. Equations (11) and (12) are first order in radius for the x and y component equations. They are integrated outward from the inner radius $r = r_{\text{in}}$ to the outer boundary $r = r_{\text{out}}$. To integrate these four equations we need to specify the four variables at the inner radius and the eigenvalue ω . Two starting conditions are supplied by the boundary condition of Equation (4), $G_x(r_{\text{in}}) = G_y(r_{\text{in}}) = 0$. We can freely specify one component of ℓ at the inner boundary and set $\ell_x(r_{\text{in}}) = 1$. The remaining quantities are $\ell_y(r_{\text{in}})$ and ω whose values are adjusted to satisfy the outer boundary condition of Equation (4), $G_x(r_{\text{out}}) = G_y(r_{\text{out}}) = 0$. There are infinitely many modes that satisfy the boundary conditions and have different values of $\ell_y(r_{\text{in}})$ and ω . To determine the nearly rigid modes, we apply initial estimates for the shooting method from analytic nearly rigid tilt modes described in Section 3 in a manner described later in Section 4.3. The calculations were performed using Mathematica software.

Table 1. Model Parameters

Model	$H/r(r_{\text{in}})$	s	p	e_{b}	α
A	0.1	0.5	1.0	0.5	0.01
B	0.05	0.5	1.0	0.5	0.01
C	0.1	1.0	1.0	0.5	0.01
D	0.1	0.5	0.5	0.5	0.01
E	0.1	0.5	1.0	0.75	0.01
F	0.1	0.5	1.0	0.5	0.05

4.2 Disc Models

We determine the linear modes for a set of disc models, all of which involve an equal mass binary. We analyze discs whose parameters are listed in Table 1, where s and p are defined by $T(r) \propto r^{-s}$ and $\Sigma(r) \propto r^{-p}$, respectively. We regard Model A as a fiducial model and consider single parameter departures from that model in other models. Models A, B, D, E, and F involve flared discs that have a disc aspect ratios $H/r \propto r^{1/4}$. Such a level of flaring (or more) is expected in so-called ‘passive’ protostellar discs, where the heating is dominated by the contributions from the central stars at all radii, or in active discs on scales greater than ~ 1 AU (Chiang & Goldreich 1997). Model C has a constant disc aspect ratio H/r . Observations of protostellar discs suggest that the surface density parameter power law exponent p is in the range of 0.5 to about 1, although there is considerable uncertainty (Williams & Cieza 2011). Model D has $p = 0.5$, while other models have $p = 1.0$.

4.3 Tilt Evolution Rates

For each disc model in Table 1 with outer disc edge r_{out} set to $50a_{\text{b}}$, we compute sequences of modes with various disc inner radii starting with large values of r_{in} . To calculate the longest lived modes, we determine the values of $\ell_{\text{y}}(r_{\text{in}})$ and ω for the large value of $r_{\text{in}} = 49a_{\text{b}}$ using the nearly rigid tilt approximation of Section 3. At such radii, the tidal field is weak and the approximation holds with high accuracy. We use those values as initial guesses for the shooting method with $r_{\text{in}} = 49a_{\text{b}}$. The shooting method converges rapidly and determines the numerically calculated eigenmode. We then apply the numerically determined values of $\ell_{\text{y}}(r_{\text{in}})$ and ω obtained by the shooting method iteratively as initial guesses for successively smaller values of r_{in} , where the approximations made in Section 3 may not hold with good accuracy.

Figure 2 plots the damping rates of tilt departures from the polar direction as a function of disc inner radius for the various models listed in Table 1. The numerically determined

damping rates are plotted as solid lines, while the damping rates determined by the nearly rigid tilt mode approximation are plotted by the dashed lines. For larger disc inner radii, $r_{\text{in}} \gtrsim 3a_{\text{b}}$, the two sets of lines merge, as is expected because the tidal effects of the binary on the disc are weak and consequently the disc experiences little warping. At smaller values of r_{in} the two sets of curves depart substantially, indicative of significant warping which suggests that the linear equations may not be valid. We return to this point in Section 4.4. In general, substantial evolution towards polar alignment occurs for all models over the course of a typical protostellar disc lifetime of a few million years for $r_{\text{in}} \lesssim 2a_{\text{b}}$ and binary orbital periods of the order of 100 years or less.

The results plotted in Figure 2 across models qualitatively follow simple expectations. Model B generally has a more rapid damping rate than Model A because the disc is cooler and therefore experiences stronger warping because of the weaker pressure communication across the disc (see Equation (29)), as is discussed further in Section 4.5. Model C has a lower temperature at larger radii than Model A and consequently experiences stronger warping for a similar reason, resulting in a generally stronger damping. Model D has a weaker concentration of mass towards smaller radii than Model A and consequently a larger fraction of the disc mass experiences the weaker tidal effects at larger radii, resulting in weaker damping. Model E has a higher binary eccentricity than Model A, resulting in a more rapid disc precession and therefore a more rapid damping rate (see Equation (30)). Model F has a larger disc viscosity than Model A, resulting in a more rapid damping rate (see Equation (29)).

Figure 3 plots the tilt damping rates of disc Model A towards polar alignment for a fixed disc inner radius $r_{\text{in}} = 2a_{\text{b}}$ (upper panel) and $r_{\text{in}} = 3a_{\text{b}}$ (lower panel) and various disc outer radii. These modes are determined by an analogous procedure used for the determination of the modes in Figure 2. We apply as initial guesses for the shooting method the values of $\ell_y(r_{\text{in}})$ and ω by using the nearly rigid tilt approximation described in Section 3 at $r_{\text{out}} = r_{\text{in}} + 0.1a_{\text{b}}$. The disc is narrow and consequently the level of warping is expected to be small. We then apply the numerically determined solutions $\ell_y(r_{\text{in}})$ and ω obtained by the shooting method iteratively as initial guesses for successively larger values of r_{out} , where the approximations made in Section 3 may not hold with good accuracy.

For smaller disc outer radii, the nearly rigid tilt mode approximation agrees well with the numerically determined eigenvalues because the disc is somewhat narrow and therefore good radial communication is possible through pressure induced bending waves. Consequently,

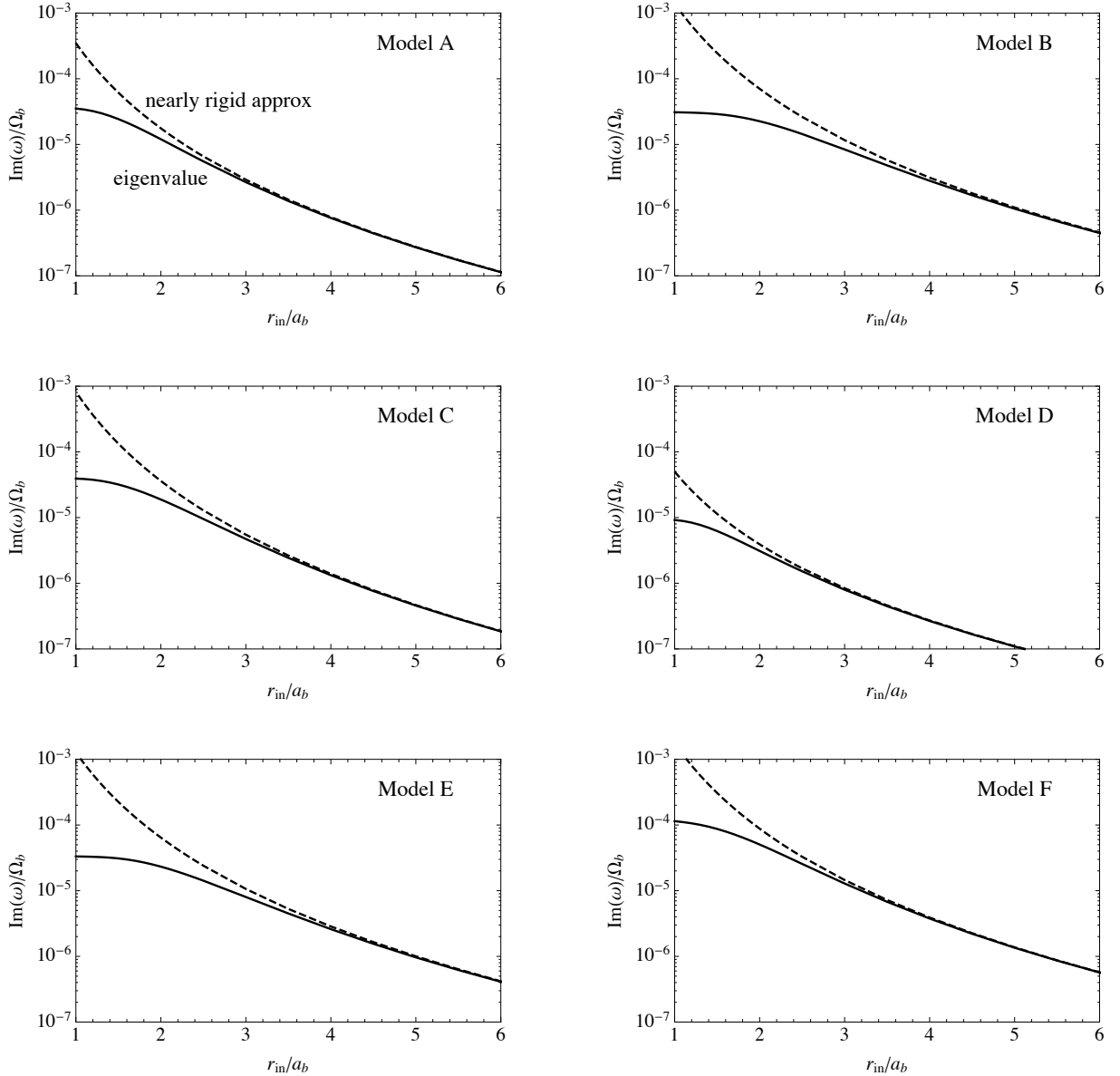


Figure 2. Semi-log plots of the rates of change of tilt towards the polar direction as a function of the disc inner radius for the various models in Table 1. The dashed line is based on the nearly rigid tilt mode approximation, Equation (28), while the solid line is based on a numerically determined eigenvalue.

there is little warping, even though the tidal forces are relatively strong. The agreement is better for the lower plot with the larger disc inner radius where the tidal forces are weaker.

Note that the damping rate in Figure 3 has a peak value for $r_{\text{out}} \sim 10a_b - 15a_b$ and is small for narrow and broad discs. To qualitatively understand this behaviour, consider Equation (28) for the tilt evolution rate $\omega^{(2)}$ in the nearly rigid tilt approximation. The $\mathbf{G}^{(1)}$ term is related to the level of warping in the disc. $\omega^{(2)}$ is then roughly related to the square of an average level of warping in the disc. For a very narrow disc, the level of warping is very small and therefore the tilt evolution rate is very small. This small level of warping occurs because the radial communication timescale through pressure induced bending waves is very short.

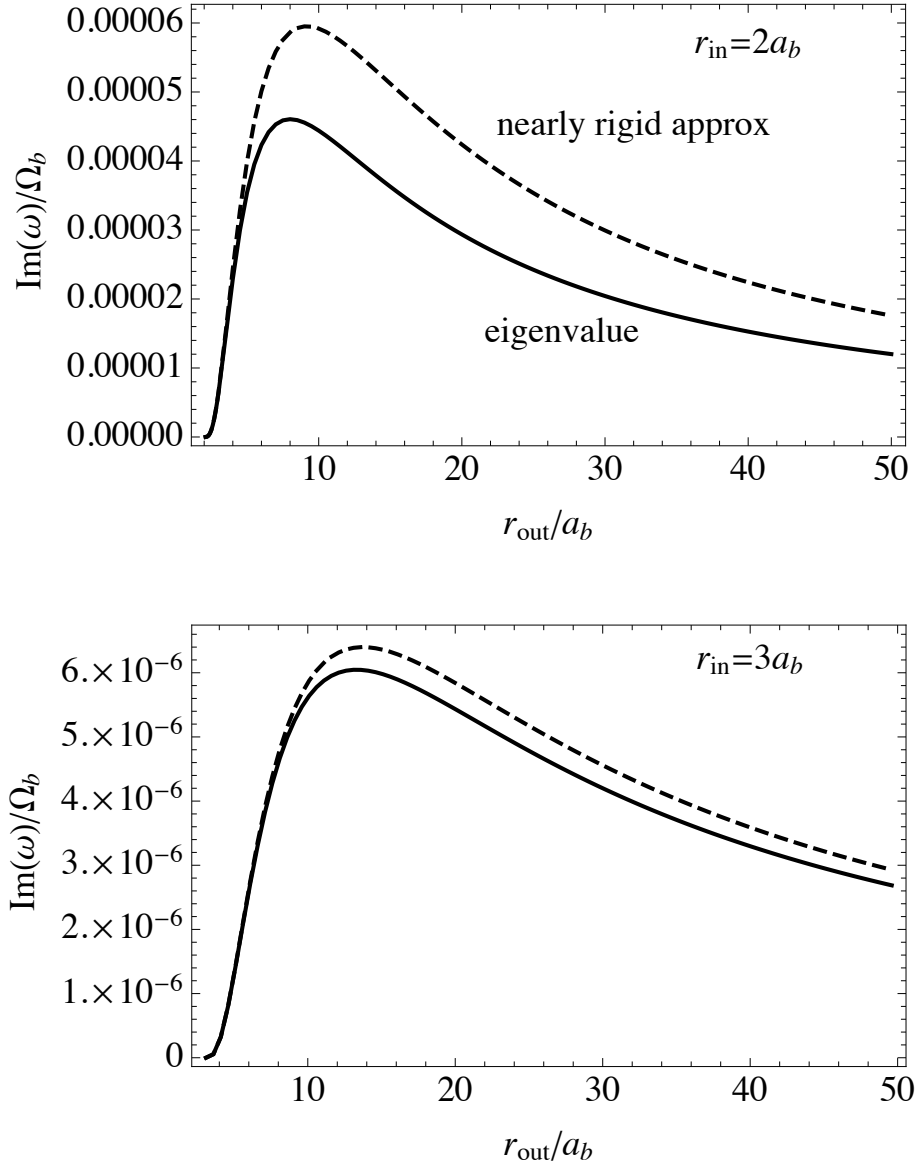


Figure 3. Linear plots of the rates of change of tilt towards the polar direction as a function of the disc outer radius for Model A in Table 1. The dashed line is based on the nearly rigid tilt mode approximation, Equation (28), while the solid line is based on a numerically determined eigenvalue. The upper (lower) panel has $r_{\text{in}} = 2a_b$ ($r_{\text{in}} = 3a_b$).

For a very broad disc, the average level of warping across the disc typically decreases with increasing disc outer radius because the outer parts of the disc experience weak torquing by the binary. Therefore for narrow discs, the tilt evolution rate increases with disc outer radius, while for very broad discs the tilt evolution rate decreases, and there is a peak at intermediate values of disc width.

4.4 Level of Warping

The tilt evolution Equations (1) and (2) are linear and derived under the assumption that the level of warping $r|d\ell/dr|$ is in some sense small. Since these equations were derived using

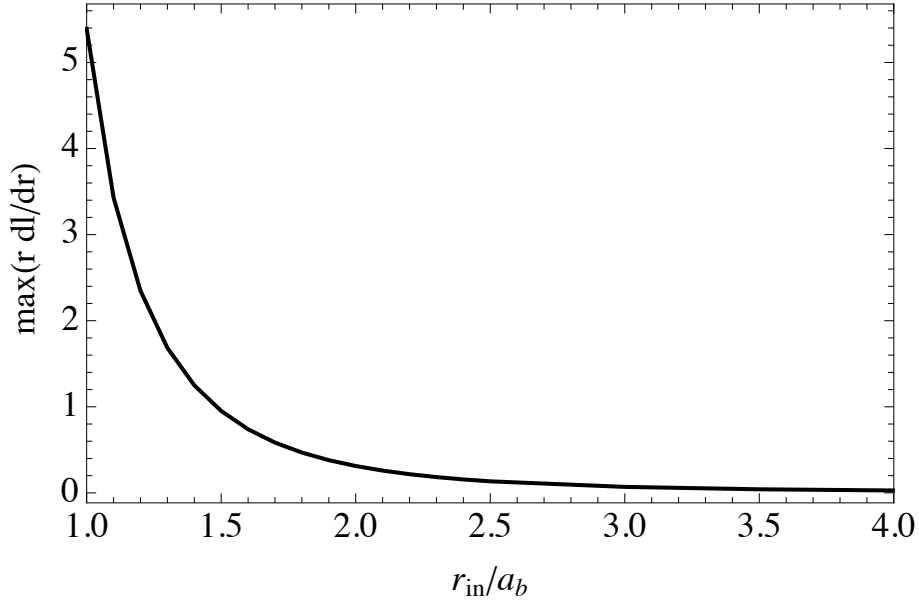


Figure 4. Maximum level of warping $r|d\ell/dr|$ across various discs as a function of their inner radii for Model A with fixed $r_{\text{out}} = 50a_b$.

Eulerian perturbations, it is not clear from their derivation where the breakdown occurs. [Ogilvie \(2006\)](#) showed that nonlinear effects cause a significant deviation in the form of the bending wave when $r|d\ell/dr| \sim (H/r)^{1/2}$ where the wave induced horizontal motions are sonic. For Model A, this implies that linearity requires that $r|d\ell/dr| \lesssim 0.3$.

Figure 4 plots the level of maximum warping across various discs as a function of their inner radii for Model A with fixed $r_{\text{out}} = 50a_b$ which applies to the upper left panel of Figure 2. For disc inner radii smaller than about $2a_b$ this linearity requirement appears to be violated. Figure 5 shows that the violation occurs close to the disc inner radius where tidal forces are strong. Note that $d\ell/dr = 0$ at $r = r_{\text{in}}$ and $r = r_{\text{out}}$ due to boundary condition Equation (4).

For smaller r_{in} , the maximum level of warping rises steeply with decreasing r_{in} , $\max(r|d\ell/dr|) \sim r^{-4}$, as determined by a rough fit to the numerically determined values. At smaller r , $\max(r|d\ell/dr|) \sim r^{-4}$ also for Models C, D, and F in Figure 2. For Models B and E, the level of warping increases more strongly with decreasing r_{in} , $\max(r|d\ell/dr|) \sim r^{-8}$. This rapid increase of warping at smaller r_{in} suggests that nonlinearity may be important even if a small fraction of the disc mass lies at such radii.

Figure 6 plots the level of maximum warping across various discs as a function of their outer radii for Model A with fixed $r_{\text{in}} = 2a_b$, which applies to the upper panel of Figure 3. In this case, the level of warping is small for narrow discs where good radial communication is possible through pressure induced bending waves. For discs with larger disc outer radii, the

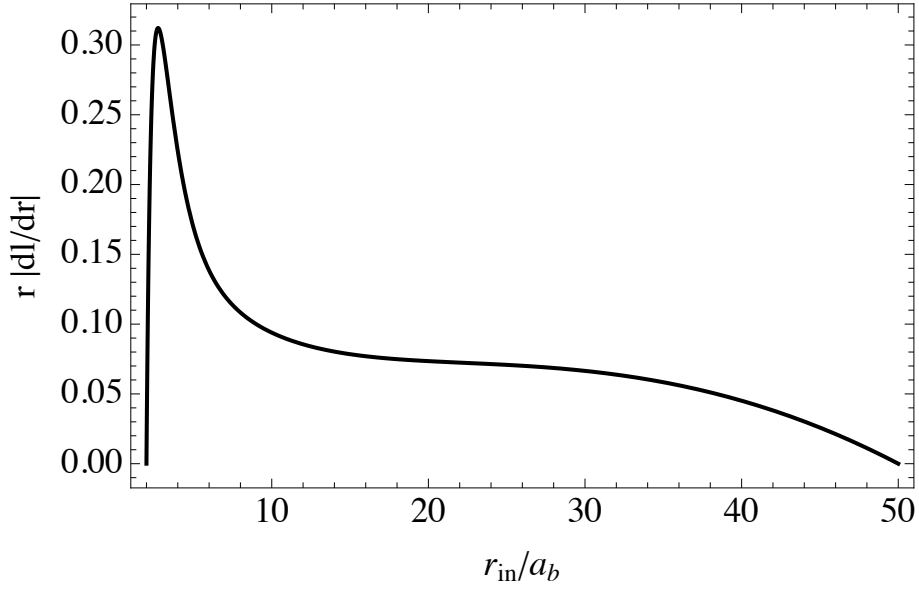


Figure 5. Level of warping $r|d\ell/dr|$ as a function of disc radius for the disc Model A with $r_{\text{in}} = 2a_b$ and $r_{\text{out}} = 50a_b$.

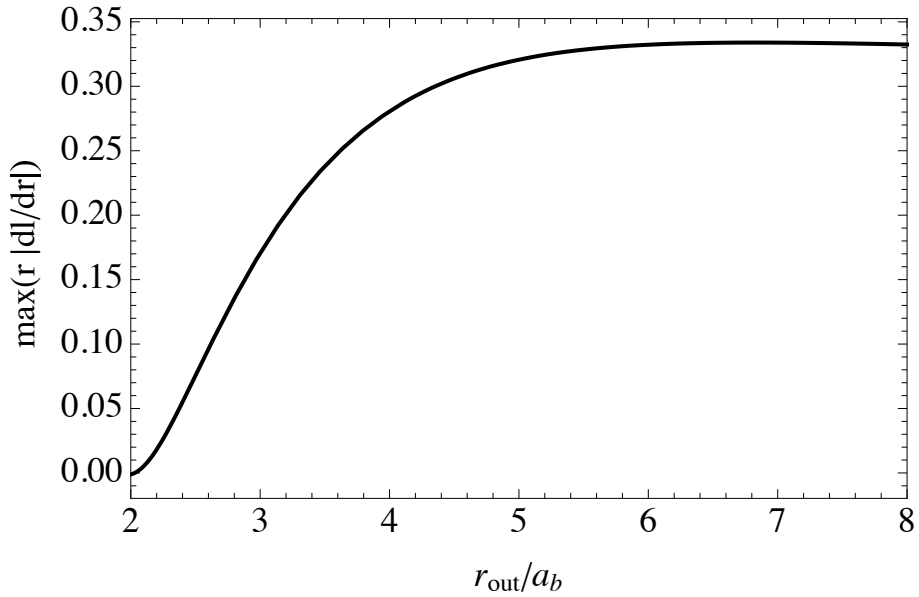


Figure 6. Maximum level of warping $r|d\ell/dr|$ across various discs as a function of the disc outer radii for Model A with fixed $r_{\text{in}} = 2a_b$.

maximum level of warping increases because the sonic communication timescale across the disc increases. However, the maximum level of warping flattens at $r \gtrsim 5a_b$ because the outer parts of the disc experience weak tidal forcing.

4.5 Approximate Criteria For Strong Warping/Breaking

In this section we consider an approximate criterion for when a broad circumbinary disc ($r_{\text{in}} \ll r_{\text{out}}$) undergoes strong warping. Strong warping could result in the disc breaking up

radially into distinct annuli (e.g., Nixon & King 2012). Estimates of breaking radii in the wave-like regime also have been made by Nixon et al. (2013) for circumbinary discs and Nealon et al. (2015) for discs around black holes. The disc maintains radial communication via pressure induced bending waves that propagate at speed $c_s/2$ for gas sound speed c_s (Papaloizou & Lin 1995; Lubow et al. 2002). This radial communication timescale is then approximately

$$t_c \approx \frac{4}{(2+s)\Omega_b h_{\text{out}}} \left(\frac{r_{\text{out}}}{a_b} \right)^{3/2}, \quad (31)$$

where h_{out} is the disc aspect ratio at the disc outer edge.

As we find in Appendix A, in the quadrupole approximation for the binary potential, the nodal precession rate for a test particle can generally be written as

$$\omega_n(r) = k \left(\frac{a_b}{r} \right)^{7/2} \Omega_b, \quad (32)$$

where k is constant in r that depends on the binary mass ratio and eccentricity and disc relative orientation. We determine global precession rate of a disc by taking its angular momentum average of ω_n , as indicated by Equation (16). As in Section 4.2, we consider discs whose density varies in r as $\Sigma \propto 1/r^p$, for some constant $0.5 \leq p \leq 1$. We take the precession timescale t_p to be the inverse of the global precession rate and obtain for $r_{\text{in}} \ll r_{\text{out}}$

$$t_p = \frac{2(1+p)r_{\text{in}}^{1+p} r_{\text{out}}^{5/2-p}}{|k|(5-2p)a_b^{7/2}\Omega_b}. \quad (33)$$

On timescale t_p , the disc would under differential precession resulting in strong warping or breaking in the absence of radial communication. Breaking can occur for a disc whose inner radius is sufficiently small that that $t_c > t_p$. By equating the precession timescale t_p to the sonic communication timescale t_c , the breaking inner disc radius in the wave-like regime is then estimated as

$$r_{\text{break}} \approx \left(\frac{2(5-2p)|k|}{h_{\text{out}}(2+s+2p+ps)} \left(\frac{a_b}{r_{\text{out}}} \right)^{1-p} \right)^{\frac{1}{1+p}} a_b \quad (34)$$

(see also Nixon et al. 2013, for the viscous regime where $\alpha > H/r$). Notice that in the case $p = 1$ as in Model A, we have that r_{break} is independent of the disc outer radius r_{out} for fixed h_{out} .

For a nearly coplanar disc with $p = 1$ and $s = 0.5$ that orbits a circular binary with equal mass component stars, we have from Equation (A17) that $k = 3/16$ and therefore $r_{\text{break}} \approx 1.5(0.1/h_{\text{out}})^{1/2} a_b$. For $p = 0.5$, $s = 0.5$, and $r_{\text{out}} = 50a_b$, we have that $r_{\text{break}} \approx 0.7(0.1/h_{\text{out}})^{2/3} a_b$. For $H/r \sim 0.1$ as can occur in the protostellar disc case, breaking does not

appear to be likely because the breaking radius is typically smaller than the tidal inner truncation radius of a circumbinary disc determined by Artymowicz & Lubow (1994) (hereafter AL94).

For a nearly polar disc that follows Model A with equal mass component stars and $e_b = 0.5$, we have from Equation (16) that $k \approx 0.30$ and therefore $r_{\text{break}} \approx 1.9(0.1/h_{\text{out}})^{1/2}a_b$. In Figure 4 the breaking radius is expected to occur where the maximum level of warping is of order unity. To apply this relation to Figure 4, we use the fact that $h_{\text{out}} = 0.1(50a_b/r_{\text{break}})^{1/4}$ for Model A. We then predict that $r_{\text{break}} \approx 1.2a_b$, where the maximum level of warping is ~ 2.5 in the figure, in rough agreement with expectation that the level of warping is of order unity. For $p = 0.5$, $s = 0.5$, and $r_{\text{out}} = 50a_b$ we have that $r_{\text{break}} \approx 0.9(0.1/h_{\text{out}})^{2/3}a_b$.

4.6 Contributions to Tilt Evolution Rate

There are two contributions to the rate of change of tilt towards polar, $Im(\omega)$ in Equation (24). One contribution involves a tidal torque term, the first term on the RHS of Equation (24), and another contribution is due an internal torque \mathbf{G} term, the second term on the RHS. We showed in Section 3.2 that the tidal torque contribution should be much smaller than the internal torque contribution, since the former vanishes to two orders in the nearly rigid tilt expansion based on the weakness of the tidal field, while the latter does not vanish at this order. In Figure 7 we plot the contributions involving these two terms to the tilt evolution rate $Im(\omega)$ using the results of the numerically determined modes for disc Model A. The plot is for the same case shown in the upper left panel of Figure 2. The contributions from the tidal term rise for smaller disc inner radii where the tidal field becomes stronger. As expected, its contributions are much smaller than those of the internal torque term, but are not vanishingly small.

5 INNER TRUNCATION OF A POLAR DISC

5.1 Role of Resonances

The inner tidal truncation of coplanar circumbinary discs involving eccentric orbit binaries is likely dominated by the effects of eccentric Lindblad resonances (AL94). At such resonances, waves are launched that carry angular momentum. As the waves damp, the angular momentum carried by the waves is transferred to the disc (Goldreich & Tremaine 1979). The gap opening condition is that the outward Lindblad resonant torque exceeds the inward viscous

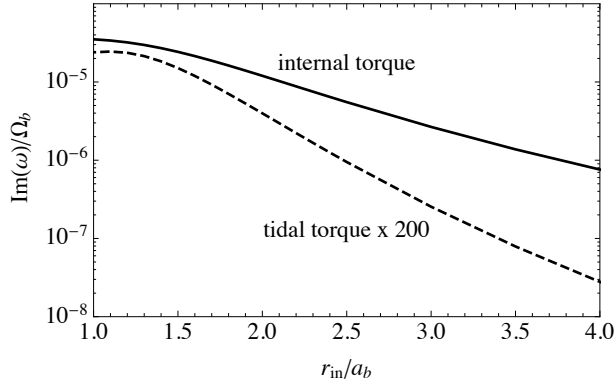


Figure 7. Semi-log plot of the contributions to the tilt evolution rate towards polar orientation as a function of disc inner radius r_{in} for fixed disc outer radius $r_{\text{out}} = 50a_b$ with disc Model A. The solid line is the contribution due to the disc internal torque \mathbf{G} term on the RHS of Equation (24) and the dashed line is the contribution due to the binary torque $\boldsymbol{\tau}$ term multiplied by 200.

torque. There are infinitely many Lindblad resonances at various radii in a circumbinary disc. The outermost (weakest) Lindblad resonance in a circumbinary disc that satisfies the gap opening condition is the one that controls the circumbinary disc inner truncation. In the case that the waves damp rapidly near the resonance, this outermost resonance location determines the circumbinary disc inner radius.

AL94 determined circumbinary disc inner radii by this procedure for discs that are coplanar and rotate in the same sense as the central binary. For tilted circumbinary discs with respect to the orbital plane of the binary, the Lindblad resonance torques are weaker than the coplanar case, resulting in a decreasing central hole size with tilt (Nixon & Lubow 2015; Miranda & Lai 2015). The reasons for the decrease are that the disc can lie farther away from the binary in the noncoplanar case and also because the relative speeds of the disc and binary increases with tilt.

5.2 Torque Equation

We determine the resonant torque exerted on a polar circumbinary disc due to an eccentric binary. We closely follow the approach of Nixon & Lubow (2015) that was applied to counter rotating discs. This approach has advantages over previous methods (e.g., Goldreich & Tremaine 1980; Artymowicz & Lubow 1994; Miranda & Lai 2015) that perform expansions in the binary eccentricity that is not generally small for binaries. The calculation of the resonant torque involves a Fourier transform of the potential in time. The expansion was used because there does not exist an explicit analytic expression for instantaneous radius of the binary orbit in terms of the binary mean anomaly (time). The approach we apply, based on Moorhead & Adams (2008), determines the resonant torque directly numer-

ically without performing an expansion in eccentricity. The advantage comes about because the instantaneous radius of the binary can be expressed explicitly in terms of its eccentric anomaly that is used as a variable, instead of mean anomaly that was used previously. The Fourier transform is expressed in terms of the eccentric anomaly, rather than time.

We adopt a cylindrical coordinate system (r, θ, z) whose origin is at the center of mass and so the $z = 0$ plane coincides with the disc midplane. Following [Goldreich & Tremaine \(1979\)](#), we decompose the potential as

$$\Phi(r, \theta, t) = \sum_{l,m} \Phi_{l,m}(r) \cos(m\theta - l\Omega_b t), \quad (35)$$

where l (not to be confused with disc tilt vector $\boldsymbol{\ell}$) and m range over integers (zero, and positive), and $\Omega_b > 0$. The binary potential has contributions from the primary star of mass M_1 and the secondary star of mass M_2 . We determine the potential components $\Phi_{l,m}$ for $l > 0$ and $m \geq 0$ by

$$\Phi_{\ell,m}(r) = \Phi_{l,m}^{(1)}(r) + \Phi_{l,m}^{(2)}(r), \quad (36)$$

where the superscripts 1 and 2 denote the primary and secondary objects. We invert Equation (35) by using the eccentric anomaly of the binary orbit ζ as a variable of integration in place of the mean anomaly, $\Omega_b t$. For a disc that is tilted with respect to the binary orbital plane by angle ψ about the axis defined by $\mathbf{e}_b \times \mathbf{J}_b$, we then have for $i = 1, 2$

$$\Phi_{l,m}^{(i)}(r) = -\frac{GM_i}{2\pi^2 a_b} \left(1 - \frac{\delta_{m,0}}{2}\right) \int_0^{2\pi} d\theta \int_0^{2\pi} d\zeta \frac{(1 - e_b \cos \zeta) \cos(m\theta - \ell(\zeta - e_b \sin \zeta))}{\sqrt{v^2 + x_i^2 (1 - e_b \cos \zeta)^2 - 2v x_i g(\theta, \zeta)}}, \quad (37)$$

where

$$g(\theta, \zeta) = \cos(\psi)(\cos \zeta - e_b) \cos(\theta) + \sqrt{1 - e_b^2} \sin(\zeta) \sin(\theta), \quad (38)$$

$x_1 = -M_2/(M_1 + M_2)$ and $x_2 = M_1/(M_1 + M_2)$ and $v = r/a_b$. For a polar disc $\psi = \pi/2$, while for a coplanar disc $\psi = 0$.

The outer Lindblad resonances in a Keplerian circumbinary disc occur where

$$\Omega(r_{l,m}) = \frac{l\Omega_b}{m+1}. \quad (39)$$

5.3 Results

The eccentric outer Lindblad resonance with $(l, m) = (1, 2)$ that occurs where $\Omega(r) = \Omega_b/3$ (via Equation (39)) plays an important role in the inner truncation of circumbinary discs of moderate viscosity and eccentricity (AL94). It is the outermost first order eccentric Lindblad resonance. For such a resonance, the torque varies quadratically in e_b for $e_b \ll 1$. Resonances

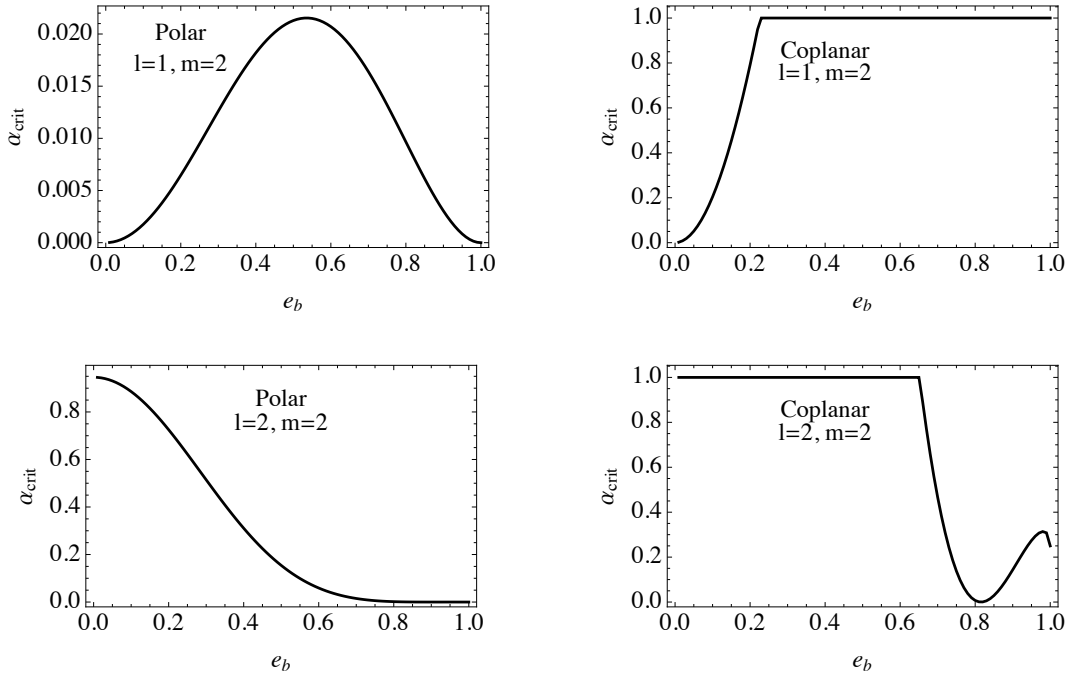


Figure 8. Critical values of viscosity parameter α as a function of binary eccentricity for the $(l, m) = (1, 2)$ and $(2, 2)$ Lindblad resonances that occur at $\Omega(r) = \Omega_b/3$ and $\Omega(r) = 2\Omega_b/3$, respectively, for equal mass binary components with disc aspect ratio $H/r = 0.1$ at the resonance.

that occur at larger radii involve torques that vary as higher powers of e_b and are weaker for $e_b \ll 1$. The outer Lindblad resonance with $(l, m) = (2, 2)$ that occurs where $\Omega(r) = 2\Omega_b/3$ is closer to the binary. It is the outermost noneccentric Lindblad resonance for an equal mass binary. Since it is closer to the binary than the $(1, 2)$ resonance, its effects on disc truncation are expected to be stronger.

Using Equation (16) of AL94 that balances viscous with resonant torques, we determine the critical viscosities α_{crit} by

$$\alpha_{\text{crit}} = \min \left(\pi m \left(\frac{\Phi_{\ell, m}}{GM/a_b} \frac{(m+1)^{1/6} (3m+1) r}{3l^{2/3} H} \right)^2, 1 \right), \quad (40)$$

where $\Phi_{\ell, m}$ is given by Equations (36) and (37). For $\alpha < \alpha_{\text{crit}}$ the resonant torque is able to open a gap in the disc. The *min* is taken in Equation (40) because values of α greater than unity are unphysical. The application of these results to tilted discs in the wavelike regime that we consider in this paper further requires that $\alpha < H/r$.

We apply Equation (40) to the $(1, 2)$ and $(2, 2)$ resonances. Figure 8 plots the α_{crit} values for this resonance as a function of binary eccentricity for disc aspect ratio $H/r = 0.1$ and equal mass binary component stars in both the polar and coplanar cases. The α_{crit} values scale inversely with $(H/r)^2$, and so a thinner disc would have higher values of $\alpha_{\text{crit}} < 1$. For $(l, m) = (1, 2)$ in both the coplanar and polar cases, α_{crit} goes to zero as e_b goes to zero

because the resonant torque vanishes at $e_b = 0$ for this eccentric Lindblad resonance. For $(l, m) = (2, 2)$ in both the coplanar and polar cases, α_{crit} does not go to zero as e_b goes to zero.

In the coplanar case, the $(l, m) = (1, 2)$ resonance can truncate a disc for even fairly small values of binary eccentricity. Any value of $\alpha < 1$ can result in gap opening for $e_b > 0.25$. Tidal truncation of a polar disc at this resonance is harder to achieve, but is possible for $\alpha \sim 0.01$ and moderate values of binary eccentricity $e_b \sim 0.5$. This resonance occurs at $r \simeq 2.08a_b$. We see from Figure 4 that at this radius, a nearly polar disc marginally satisfies the conditions for the assumed linearity of the tilt evolution equations used in this paper.

In coplanar case, the $(l, m) = (2, 2)$ resonance can generally truncate the disc, for any value of $\alpha < 1$, for $e_b \lesssim 0.7$. α_{crit} vanishes near $e_b = 0.8$ because the potential component $\Phi_{2,2}$ vanishes near there. In polar case, α_{crit} for the $(l, m) = (2, 2)$ resonance declines with increasing binary eccentricity.

In both polar cases, α_{crit} decreases at larger eccentricity as the binary orbit becomes more elongated. In the extreme polar case of $e_b = 1$, the binary orbit takes the form of a line that lies perpendicular to the disc plane and provides an axisymmetric potential in the disc plane. Thus, the torque must vanish in that case, as seen in the left panels of Figure 8. By this argument, it follows that all resonant tidal torques vanish for $e_b = 1$. Consequently, we expect that a highly eccentric binary is unlikely to be able to efficiently tidally truncate a polar disc. As a result, the polar circumbinary disc will likely undergo strong warping and possibly breaking at smaller radii.

6 UNSTABLE PERPENDICULAR CONFIGURATION

Stationary test particle orbits in the inertial frame around an eccentric binary exist for coplanar and polar orbit orientations. They are related to the stable circumbinary disc configuration for the coplanar case (Facchini et al. 2013; Foucart & Lai 2014) and also for the polar state as we saw in Section 3.2. In the coplanar and polar cases, discs undergo nodal precession for the small departures from a coplanar/polar state. They evolve towards their final states due to the effects of dissipation. As pointed out by Farago & Laskar (2010), there is an orthogonal direction of particle angular momentum, along $\mathbf{J}_b \times \mathbf{e}_b$, for which test particle orbits are stationary in the inertial frame, but are unstable. To investigate the disc evolution in that case, we proceed along the lines of the analysis in Section 2.

We take the x -axis to be along \mathbf{J}_b and the z -axis to be along $\mathbf{J}_b \times \mathbf{e}_b$ and apply equations (2.16) and (2.18) in Farago & Laskar (2010). For the torque defined in Equation (5) we then have

$$a(r) = 5e_b^2 \omega_p(r) \quad (41)$$

and

$$b(r) = (1 - e_b^2) \omega_p(r), \quad (42)$$

with ω_p again given by Equation (9). Note that we apply a different coordinate system in which our (x, y, z) coordinates corresponds to their (z, x, y) coordinates. The binary orbit lies in the $y - z$ plane. In the rigid tilt expansion in analogy with Equation (16) for the polar case, we have

$$\omega^{(1)} = \pm i \frac{3\sqrt{5}}{4} e_b \sqrt{1 - e_b^2} \frac{M_1 M_2}{M^2} \Omega_b \left\langle \left(\frac{a_b}{r} \right)^{7/2} \right\rangle. \quad (43)$$

In this case, $\omega^{(1)}$ is imaginary and therefore corresponds to an unstable tilt evolution in lowest order. Independent of the results at next order, the disc generally undergoes growing deviations of tilt away from the perpendicular state.

For this perpendicular configuration, the first term on the RHS of Equation (25) is nonzero in first order and dominates over the second term. This behaviour is quite different from the polar case where this term is zero to second order.

7 ENERGETICS

As noted in the Introduction, a circumbinary test particle orbit of fixed radius that is nearly coplanar to a binary and subject to some form of dissipation would be expected to become coplanar, based on the idea that the coplanar orbit has the least energy. However, the polar case is at a global energy maximum for particle orbits of fixed radius over all possible orbital orientations. This can be seen from the Hamiltonian given by Equation (2.13) of Farago & Laskar (2010) for which the polar case has tilt $i_2 = \pi/2$ and longitude of ascending node $\Omega_2 = \pi/2$ in their notation. The coplanar case ($i_2 = 0$) is at a global energy minimum and the perpendicular case of Section 6 ($i_2 = \pi/2$, $\Omega_2 = 0$) is intermediate.

This somewhat counter intuitive result that polar orbits are stable at energy maxima has been examined in the context of a possible polar ring around Neptune by Dobrovolskis et al. (1989). They describe a somewhat simplified case of a viscous ring around a spheroid that is axisymmetric about the polar axis, rather than the triaxial ellipsoid case with unequal axes

that applies to an eccentric binary. However, the main physical point is relevant. Based on angular momentum conservation in the polar direction, they show that such a nearly polar ring must contract (accrete) as it achieves a polar orientation. Therefore, the assumption of fixed radius in comparing orbital energies is not correct. When the associated ring contraction is accounted for, there is a net energy loss in evolving to the polar state.

[Dobrovolskis et al. \(1989\)](#) also point out that a viscous ring that orbits about an oblate spheroid and is initially slightly tilted with respect to spheroid's equator would be expected to evolve to the plane of the equator. This configuration is analogous to that of a circumbinary disc that is initially nearly coplanar. On the other hand, consider evolution of a viscous ring about a prolate spheroid that is initially slightly tilted with respect to its equator. This configuration is analogous to that of a circumbinary disc that is initially nearly polar. If the two cases have quadrupole moments of equal magnitude but opposite sign, then the rings undergo nodal precession in opposite directions in the two cases. But by Equation (29) applied to such systems, both cases should evolve to equatorial alignment at equal rates.

Polar secular stability is made possible because slightly tilted test particle orbits away from the polar state undergo precession and are therefore neutrally stable. Dissipational forces acting on this neutral state are able to cause evolution towards the polar state. The perpendicular state discussed in Section 6 is unstable to slight departures from the polar state. Its evolution corresponds to simple expectations of evolution from a local energy maximum.

8 SUMMARY

We have investigated the evolution of a nearly polar low mass disc around an eccentric binary by means of linear theory. Evolution towards the polar state was recently shown in SPH simulations by [Martin & Lubow \(2017\)](#). We apply the secular binary potential in the quadrupole approximation developed by [Farago & Laskar \(2010\)](#) to explore the secular evolution of a nearly polar disc by using the linear tilt evolution equations of [Lubow & Ogilvie \(2000\)](#). Unlike the circumbinary disc evolution in the circular orbit binary case, in the eccentric binary case the disc undergoes secular tilt oscillations, as well as precession (see Figure 1).

We have shown analytically in the limit of weak tidal forcing that a nearly polar circumbinary disc evolves towards the polar state through the effects of dissipation caused by

turbulent viscosity. We have determined the tilt evolution timescales by means of an analytic nearly rigid tilt expansion and by means of numerically determined modes. The two methods agree well where the disc warping is small (see Figures 2 and 3). For typical protostellar disc parameters and binary eccentricity $e_b \sim 0.5$, substantial tilt evolution can occur over a typical disc lifetime of a few million years for equal mass binaries whose orbital periods are of order 100 years or less. Estimates of evolution timescales for other parameters can be obtained using scaling relation Equation (30). The tilt evolution timescales fall rapidly with the decreasing radius of the disc inner edge. For disc inner radii of a few times the binary semi-major axis, the warping becomes strong enough that the linearity assumption begins to break down (see Figures 4 and 5).

Disc tidal truncation by means of resonance torques involving eccentric binaries is much less effective for polar discs than for coplanar discs (see Figure 8). For a binary with an eccentricity of unity, no resonant forcing of a polar disc occurs because the binary provides an axisymmetric secular potential in the disc plane. The results suggest then that polar disc material in Keplerian orbits may sometimes reach to small enough disc radii that nonlinear effects may play an important role.

For fixed orbital radius, polar orbits are at an energy maximum, while coplanar orbits are at an energy minimum. In Section 7, we describe how disc evolution to a polar state is energetically possible.

In this analysis we have considered only low mass discs, whose angular momenta are small compared to that of their central binary. For discs of larger mass, the gravitational and accretion torques exerted by the disc on the binary can have an important influence on the binary orbital evolution. As noted in Martin & Lubow (2017), such effects can reduce the binary eccentricity that may in turn suppress disc polar alignment.

The results show that circumbinary discs can evolve to polar states, such as found in observations of binary 99 Herculis (Kennedy et al. 2012). Circumbinary planets might then form in such discs and reside on polar orbits. The long term stability of planets on such orbits needs to be understood. The analytic model of Farago & Laskar (2010) suggests that polar orbits of test particles are stable. However, this model is based on the quadrupole approximation for the binary potential. Doolin & Blundell (2011) carried out direct test particle orbit integrations. Their results revealed that polar orbits are stable over timescales of 5×10^4 binary orbits (the maximum timescale of their simulations) for order unity mass

ratio binaries with eccentricities of a tenth or more, if the orbital radius is greater than a few times the binary semi-major axis.

REFERENCES

- Aly H., Dehnen W., Nixon C., King A., 2015, *MNRAS*, **449**, 65
- Artymowicz P., Lubow S. H., 1994, *ApJ*, **421**, 651
- Bate M. R., 2012, *MNRAS*, **419**, 3115
- Bate M. R., Lodato G., Pringle J. E., 2010, *MNRAS*, **401**, 1505
- Bonnell I., Bastien P., 1992, *ApJ*, **401**, 654
- Brinch C., Jørgensen J. K., Hogerheijde M. R., Nelson R. P., Gressel O., 2016, *ApJ*, **830**, L16
- Capelo H. L., Herbst W., Leggett S. K., Hamilton C. M., Johnson J. A., 2012, *ApJ*, **757**, L18
- Cazzoletti P., Ricci L., Birnstiel T., Lodato G., 2017, *A&A*, **599**, A102
- Chiang E. I., Goldreich P., 1997, *ApJ*, **490**, 368
- Chiang E. I., Murray-Clay R. A., 2004, *ApJ*, **607**, 913
- Combes F., 2014, in Iodice E., Corsini E. M., eds, *Astronomical Society of the Pacific Conference Series Vol. 486, Multi-Spin Galaxies*. p. 207 ([arXiv:1312.6475](https://arxiv.org/abs/1312.6475))
- Dobrovolskis A. R., Borderies N. J., Steiman-Cameron T. Y., 1989, *Icarus*, **81**, 132
- Doolin S., Blundell K. M., 2011, *MNRAS*, **418**, 2656
- Doyle L. R., et al., 2011, *Science*, **333**, 1602
- Durisen R. H., Tohline J. E., Burns J. A., Dobrovolskis A. R., 1983, *ApJ*, **264**, 392
- Facchini S., Lodato G., Price D. J., 2013, *MNRAS*, **433**, 2142
- Farago F., Laskar J., 2010, *MNRAS*, **401**, 1189
- Foucart F., Lai D., 2013, *ApJ*, **764**, 106
- Foucart F., Lai D., 2014, *MNRAS*, **445**, 1731
- Goldreich P., Tremaine S., 1979, *ApJ*, **233**, 857
- Goldreich P., Tremaine S., 1980, *ApJ*, **241**, 425
- Iodice E., et al., 2015, *A&A*, **583**, A48
- Kennedy G. M., et al., 2012, *MNRAS*, **421**, 2264
- Kostov V. B., et al., 2016, *ApJ*, **827**, 86
- Larwood J. D., Papaloizou J. C. B., 1997, *MNRAS*, **285**, 288
- Li D., Zhou J.-L., Zhang H., 2014, *MNRAS*, **437**, 3832
- Lodato G., Facchini S., 2013, *MNRAS*, **433**, 2157
- Lubow S. H., 1992, *ApJ*, **398**, 525
- Lubow S. H., Ogilvie G. I., 2000, *ApJ*, **538**, 326
- Lubow S. H., Ogilvie G. I., 2001, *ApJ*, **560**, 997
- Lubow S. H., Ogilvie G. I., Pringle J. E., 2002, *MNRAS*, **337**, 706
- Martin R. G., Lubow S. H., 2017, *ApJ*, **835**, L28
- Miranda R., Lai D., 2015, *MNRAS*, **452**, 2396
- Moorhead A. V., Adams F. C., 2008, *Icarus*, **193**, 475
- Nealon R., Price D. J., Nixon C. J., 2015, *MNRAS*, **448**, 1526
- Nixon C. J., King A. R., 2012, *MNRAS*, **421**, 1201
- Nixon C., Lubow S. H., 2015, *MNRAS*, **448**, 3472
- Nixon C. J., King A. R., Pringle J. E., 2011, *MNRAS*, **417**, L66
- Nixon C., King A., Price D., 2013, *MNRAS*, **434**, 1946

- Offner S. S. R., Kratter K. M., Matzner C. D., Krumholz M. R., Klein R. I., 2010, *ApJ*, **725**, 1485
- Ogilvie G. I., 2006, *MNRAS*, **365**, 977
- Papaloizou J. C. B., Lin D. N. C., 1995, *ApJ*, **438**, 841
- Papaloizou J. C. B., Pringle J. E., 1983, *MNRAS*, **202**, 1181
- Papaloizou J. C. B., Terquem C., 1995, *MNRAS*, **274**, 987
- Schweizer F., Whitmore B. C., Rubin V. C., 1983, *AJ*, **88**, 909
- Steiman-Cameron T. Y., Durisen R. H., 1990, *ApJ*, **357**, 62
- Tokuda K., et al., 2014, *ApJL*, **789**, L4
- Welsh W. F., et al., 2015, *ApJ*, **809**, 26
- Whitmore B. C., Lucas R. A., McElroy D. B., Steiman-Cameron T. Y., Sackett P. D., Olling R. P., 1990, *AJ*, **100**, 1489
- Williams J. P., Cieza L. A., 2011, *ARA&A*, **49**, 67
- Winn J. N., Holman M. J., Johnson J. A., Stanek K. Z., Garnavich P. M., 2004, *ApJ*, **603**, L45
- Zanazzi J. J., Lai D., 2017, preprint, ([arXiv:1706.07823](https://arxiv.org/abs/1706.07823))

APPENDIX A: PRECESSION RATES

We consider a massless particle orbiting a central binary with components of mass M_1 and M_2 and total mass $M = M_1 + M_2$, semi-major axis a_b , the angular frequency $\Omega_b = \sqrt{GM/a_b^3}$, and eccentricity e_b . The particle is taken to be on a circular orbit around the binary. We work in a frame in which the angular momentum of the binary is along the z -axis and the eccentricity vector of the binary is along the x -axis. The position of the particle relative to the barycentre of the binary is $\mathbf{r}_p = (x, y, z)$. The particle is at a distance $r_p = \sqrt{x^2 + y^2 + z^2}$. The instantaneous difference in positions of the binary components is denoted by \mathbf{r}_b .

Assuming that $r_b \ll r_p$, the gravitational potential due to the binary is given by

$$\Phi = \Phi_K + \Phi_p, \quad (\text{A1})$$

where

$$\Phi_K = -\frac{GM}{r_p} \quad (\text{A2})$$

is the Keplerian potential and

$$\Phi_p = -\frac{G\beta}{2r_p^3} \left[3\frac{(\mathbf{r}_p \cdot \mathbf{r}_b)^2}{r_p^2} - r_b^2 \right] \quad (\text{A3})$$

is the lowest order (quadrupole) perturbing potential and the reduced mass is

$$\beta = \frac{M_1 M_2}{M_1 + M_2}. \quad (\text{A4})$$

In order to determine the secular evolution, we need to average the perturbing potential over the mean anomaly (time) for the orbits of the binary and the particle. We first consider the time average over the binary orbit. As shown in [Farago & Laskar \(2010\)](#),

$$\langle \mathbf{r}_b \cdot \mathbf{r}_p \rangle^2 = \frac{a_b^2}{2}(x^2 + y^2) + \frac{a_b^2 e_b^2}{2}(4x^2 - y^2) \quad (\text{A5})$$

and

$$\langle r_b^2 \rangle = a_b^2 \left(1 + \frac{3}{2} e_b^2 \right). \quad (\text{A6})$$

The binary orbit time-averaged potential is then

$$\langle \Phi_p \rangle = - \frac{a_b^2 G \beta \left[(1 + 9e_b^2)x^2 + (1 - 6e_b^2)y^2 - (2 + 3e_b^2)z^2 \right]}{4(x^2 + y^2 + z^2)^{5/2}}. \quad (\text{A7})$$

We define a new coordinate system in which the z' axis is along the angular momentum vector of the particle,

$$\boldsymbol{\ell}_3 = \boldsymbol{\ell}_p = (\ell_x, \ell_y, \ell_z). \quad (\text{A8})$$

The unit vector along the direction of angular momentum of the binary $\boldsymbol{\ell}_b = (0, 0, 1)$ in the original coordinate system. The new y' axis is in the direction

$$\boldsymbol{\ell}_2 = \frac{\boldsymbol{\ell}_b \times \boldsymbol{\ell}_p}{|\boldsymbol{\ell}_b \times \boldsymbol{\ell}_p|} = \left(-\frac{\ell_y}{\sqrt{\ell_x^2 + \ell_y^2}}, \frac{\ell_x}{\sqrt{\ell_x^2 + \ell_y^2}}, 0 \right) \quad (\text{A9})$$

and the x' axis is in the direction

$$\boldsymbol{\ell}_1 = \frac{\boldsymbol{\ell}_2 \times \boldsymbol{\ell}_3}{|\boldsymbol{\ell}_2 \times \boldsymbol{\ell}_3|}. \quad (\text{A10})$$

We can convert the angular momentum of the particle to the new coordinate system with

$$\mathbf{r}'_p = (x', y', z') = (\mathbf{r}_p \cdot \boldsymbol{\ell}_1, \mathbf{r}_p \cdot \boldsymbol{\ell}_2, \mathbf{r}_p \cdot \boldsymbol{\ell}_3). \quad (\text{A11})$$

We solve this equation to find x , y and z in terms of x' , y' and z' .

We work in plane polar coordinates in the plane of the circular particle orbit and set $x' = r \cos \phi$, $y' = r \sin \phi$ and $z' = 0$. In order to average the potential over the mean anomaly of the particle, we average over ϕ and obtain

$$\langle \langle \Phi_p \rangle \rangle = \frac{G\beta a_b^2}{8r^3} \left[3e_b^2 \left(4\ell_x^2 - \ell_y^2 - 1 \right) + 3\ell_x^2 + 3\ell_y^2 - 2 \right], \quad (\text{A12})$$

where we have eliminated ℓ_z through the identity $\ell_z^2 = 1 - \ell_x^2 - \ell_y^2$. We denote the doubly averaged potential as $\Psi = \langle \langle \Phi_K + \Phi_p \rangle \rangle$. The particle angular frequency is given by

$$\Omega^2 = \frac{1}{r} \Psi'(r) \quad (\text{A13})$$

and the epicyclic frequency

$$\kappa^2 = \frac{3}{r} \Psi'(r) + \Psi''(r), \quad (\text{A14})$$

where prime denotes differentiation. Using Equations (A1), (A2), and (A12), we then find

the apsidal precession rate is given by

$$\begin{aligned}\omega_a &= \Omega - \kappa \simeq \frac{\Omega^2 - \kappa^2}{2\Omega} \\ &\approx -\frac{3}{8}\Omega_b \left(\frac{\beta}{M}\right) \left(\frac{a_b}{r}\right)^{7/2} \left[3e_b^2 (4\ell_x^2 - \ell_y^2 - 1) + 3\ell_x^2 + 3\ell_y^2 - 2\right],\end{aligned}$$

where $\Omega = \sqrt{GM/r^3}$ is the Keplerian velocity. For a particle orbit that is close to coplanar, so that $l_x = l_y = 0$, the apsidal precession rate is given by

$$\omega_a = \frac{3}{8}\Omega_b \left(\frac{\beta}{M}\right) \left(\frac{a_b}{r}\right)^{7/2} (2 + 3e_b^2). \quad (\text{A15})$$

For a particle orbit that is close to polar, such that $\ell_x = 1$ and $\ell_y = 0$, the apsidal precession rate is given by

$$\omega_a = -\frac{3}{8}\Omega_b \left(\frac{\beta}{M}\right) \left(\frac{a_b}{r}\right)^{7/2} (1 + 9e_b^2). \quad (\text{A16})$$

For a particle orbit that is nearly coplanar about a circular orbit binary, the nodal and apsidal precession rates are nearly equal in magnitude, but opposite in sign. Therefore, from Equation (A15), the nodal precession rate about a circular orbit binary in that case is given by

$$\omega_n = -\frac{3}{4}\Omega_b \frac{\beta}{M} \left(\frac{a_b}{r}\right)^{7/2}, \quad (\text{A17})$$

which agrees with equation (2.24) of Farago & Laskar (2010) derived for a circular orbit binary with $i_2 = 0$ and $e_2 = 0$ in their notation.

APPENDIX B: EVALUATION OF UNIT VECTOR PRODUCT TERM

B1 Constancy of Unit Vector Product Term

We define quantity

$$\chi(r) = \text{Re}(\ell_x(r)\ell_y^*(r)) \quad (\text{B1})$$

and consider its derivative in first order as

$$\frac{d\chi^{(1)}}{dr} = \text{Re} \left(\frac{d\ell_x^{(1)}}{dr} \ell_y^{(0)*} + \ell_x^{(0)} \frac{d\ell_y^{(1)*}}{dr} \right). \quad (\text{B2})$$

By multiplying the x -component of Equation (21) by $\ell_y^{(0)*}$ and multiplying the y -component of Equation (21) by $\ell_x^{(0)*}$ we obtain

$$\frac{d\chi^{(1)}}{dr} = \frac{4\alpha\Omega}{\mathcal{I}r^3\Omega^3} \text{Re}(G_x^{(1)} \ell_y^{(0)*} + G_y^{(1)} \ell_x^{(0)*}). \quad (\text{B3})$$

By applying Equations (16), (18), and (20), we obtain that

$$\text{Re}(G_x^{(1)} \ell_y^{(0)*}) = \left| \ell_x^{(0)} \right|^2 \frac{\langle B^{(1)} \rangle}{\langle A^{(1)} \rangle} \int_{r_{\text{in}}}^r \Sigma r'^3 \Omega \left(A^{(1)} - \langle A^{(1)} \rangle \right) dr' \quad (\text{B4})$$

and

$$\text{Re}(G_y^{(1)} \ell_x^{(0)*}) = - \left| \ell_x^{(0)} \right|^2 \int_{r_{\text{in}}}^r \Sigma r'^3 \Omega \left(B^{(1)} - \langle B^{(1)} \rangle \right) dr', \quad (\text{B5})$$

where $\langle \rangle$ denotes the angular momentum weighted average, as was applied in Equation (17). Using the fact the $B^{(1)}(r)/A^{(1)}(r)$ is independent of r , we obtain that

$$\frac{d\chi^{(1)}}{dr} = 0 \quad (\text{B6})$$

and therefore $\chi^{(1)}$ is constant in r .

B2 Evaluation of Tilt Component at Disc Inner Edge

We consider r times Equation (11) in second order. We integrate that equation over the entire disc and apply the boundary condition Equation (4) to obtain

$$i\omega^{(2)} \ell_x^{(0)} + i\omega^{(1)} \langle \tilde{\ell}_x^{(1)} \rangle = \langle A^{(1)} \rangle \ell_y^{(1)}(r_{\text{in}}) + \langle A^{(1)} \tilde{\ell}_y^{(1)} \rangle \quad (\text{B7})$$

and

$$i\omega^{(2)} \ell_y^{(0)} + i\omega^{(1)} \ell_y^{(1)}(r_{\text{in}}) + i\omega^{(1)} \langle \tilde{\ell}_y^{(1)} \rangle = \langle B^{(1)} \tilde{\ell}_x^{(1)} \rangle, \quad (\text{B8})$$

where

$$\tilde{\ell}^{(1)}(r) = \int_{r_{\text{in}}}^r \frac{4\alpha\Omega\mathbf{G}^{(1)}}{\mathcal{I}r'^3\Omega^3} dr'. \quad (\text{B9})$$

We eliminate $\omega^{(2)}$ and solve for $\ell_y^{(1)}(r_{\text{in}})$ to obtain

$$\ell_y^{(1)}(r_{\text{in}}) = \frac{\left(\langle B^{(1)} \tilde{\ell}_x^{(1)} \rangle \ell_x^{(0)} - \langle A^{(1)} \tilde{\ell}_y^{(1)} \rangle \ell_y^{(0)} \right) + \left(\langle B^{(1)} \rangle \langle \tilde{\ell}_x^{(1)} \rangle \ell_x^{(0)} - \langle A^{(1)} \rangle \langle \tilde{\ell}_y^{(1)} \rangle \ell_y^{(0)} \right)}{2 \langle A^{(1)} \rangle \ell_y^{(0)}}. \quad (\text{B10})$$

By applying Equations (20) and (B9) we have that

$$\langle B^{(1)} \tilde{\ell}_x^{(1)} \rangle \ell_x^{(0)} = \ell_x^{(0)} \ell_y^{(0)} \int_{r_{\text{in}}}^{r_{\text{out}}} dr''' \int_{r_{\text{in}}}^{r'''} dr'' \int_{r_{\text{in}}}^{r''} dr' f(r', r'', r''') B^{(1)}(r''') \left(A^{(1)}(r') - \langle A^{(1)} \rangle \right) \quad (\text{B11})$$

and

$$\langle A^{(1)} \tilde{\ell}_y^{(1)} \rangle \ell_y^{(0)} = \ell_x^{(0)} \ell_y^{(0)} \int_{r_{\text{in}}}^{r_{\text{out}}} dr''' \int_{r_{\text{in}}}^{r'''} dr'' \int_{r_{\text{in}}}^{r''} dr' f(r', r'', r''') A^{(1)}(r''') \left(B^{(1)}(r') - \langle B^{(1)} \rangle \right) \quad (\text{B12})$$

where f is a function that is dependent of $A^{(1)}$ and $B^{(1)}$.

Using the fact that $B^{(1)}(r)/A^{(1)}(r)$ is independent of r together with Equations (B11) and (B12), we then have that the first term in parenthesis on the RHS of Equation (B10) is zero.

It similarly follows that the second term in parenthesis is also zero. Consequently,

$$\ell_y^{(1)}(r_{\text{in}}) = 0. \quad (\text{B13})$$

B3 Evaluation of the Product Term at All Radii

Using Equations (23) and (B13), we then have that

$$\chi^{(1)}(r_{\text{in}}) = \text{Re} \left(\ell_x^{(0)}(r_{\text{in}}) \ell_y^{(1)*}(r_{\text{in}}) \right) = 0. \quad (\text{B14})$$

From Equation (B6), we then have that

$$\chi^{(1)}(r) = 0 \quad (\text{B15})$$

for all r in the disc. It then follows that $\text{Re}(\ell_x(r) \ell_y^*(r)) = 0$ in first order and therefore the RHS of Equation (27) is zero.

This paper has been typeset from a $\text{\TeX}/\text{\LaTeX}$ file prepared by the author.